Nanoscale

PAPER

View Article Online
View Journal | View Issue

Cite this: *Nanoscale*, 2025, **17**, 2520

Ultralight flexible 3D nickel micromesh decorated with NiCoP for high stability alkaline zinc batteries†

Zana Karim Abdul,[a,c] Zeqi Nie,[a] Yapeng Zhang,[a] XiuXue Liu,[a] Xiaohu Wang,[a] Niwamanya Gilbert,[a] Donghai Wei, *[a,b] Wen Zhang *[d] and Guanhua Zhang [a,c]

Rechargeable alkaline zinc batteries are emerging as promising candidates for next-generation energy storage systems, owing to their affordability, eco-friendliness and high energy density. However, their widespread application is hindered by stability challenges, particularly in alkaline environments, due to cathode corrosion and deformation, as well as dendrite formation and unwanted side reactions at the Zn anode. To address these issues, we successfully developed a 3D nickel micromesh-supported NiCoP (3D NM@NiCoP) electrode. This unique structure integrates an ultrathin (4 μm), flexible and conductive nickel micromesh (NM) with a high-capacity bimetallic phosphide, NiCoP, fabricated through a combination of photolithography, chemical etching, and electro-deposition processes. The resulting electrode achieves an impressive capacitance of 26.1 μA h cm^{-2} at a current density of 4 mA cm^{-2} in a 2 M KOH electrolyte. When assembled with a superhydrophilic Zn@Al_2O_3@TiO_2 anode, the device (3D NM@NiCoP// Zn@Al_2O_3@TiO_2) exhibits outstanding stability, retaining 91% of its initial capacity after 11 000 cycles at 3 mA cm^{-2} in a 2 M KOH electrolyte. This novel configuration, with potential for scalable fabrication, provides valuable insights into the development of high-capacity and durable electrodes for alkaline zinc batteries.

Received 30th September 2024,
Accepted 28th December 2024

DOI: 10.1039/d4nr04021j

rsc.li/nanoscale

1 Introduction

In response to the growing demand for electrical vehicles and portable electronic devices, aqueous alkaline zinc batteries have emerged as a promising alternative to lithium-ion batteries due to their high safety, low cost, wide availability and environmental friendliness.[1–5] However, their low power density and unsatisfactory cycle life have hindered their widespread commercial application.[6,7] Additionally, as the demand for wearable devices continues to rise, flexible alkaline zinc batteries (FAZBs) are becoming increasingly important for wearable electronics applications.[8–10] Yet, the deficient energy density of FAZBs necessitates the urgent development of electrodes that combine desirable mechanical flexibility, large specific capacity, and robust structural stability.

Among various cathode materials, transition metal compounds have garnered significant research attention. When paired with Zn anodes in alkaline electrolytes, these devices can operate at a high output voltage of approximately 1.75 V, outperforming other aqueous batteries.[11] Nickel and cobalt are commonly utilized transition metal elements in electrochemically active materials. NiCo-based compounds—such as hydroxides, oxides, sulfides, and phosphides—showcase mixed valence states and multiple redox reactions, making them effective cathode materials for high energy storage capacity.[12–16] NiCoP, in particular, stands out due to its excellent electrical conductivity and high specific capacity, garnering considerable attention.[17–19] For instance, Zhao's group developed novel mesoporous NiCo[20] phosphate sheets on Ni foam, which, when assembled into a Ni–Zn battery with Zn foil, delivered a fairly high specific capacity of 195.5 mA h g^{-1} at a current density of 1 A g^{-1}.[21] The limited energy density may stem from inadequate exposure of the active material on the surface. To address this, various strategies have been employed to enhance the specific surface area and expose more active sites. Wang *et al.* constructed a porous microcrack

[a]*National Engineering Research Center for High-Efficiency Grinding, State Key Laboratory of Advanced Design and Manufacturing Technology for Vehicle, College of Mechanical and Vehicle Engineering, Hunan University, Changsha 410082, China. E-mail: weidonghai000@126.com, zhang.wen@auckland.ac.nz*
[b]*Hunan University of Technology, Zhuzhou 412008, China*
[c]*Greater Bay Area Institute for Innovation, Hunan University, Guangzhou 511300, China*
[d]*Department of Chemical and Materials Engineering, the University of Auckland, Auckland CBD, Auckland 1142, New Zealand*
† Electronic supplementary information (ESI) available. See DOI: https://doi.org/10.1039/d4nr04021j

NiCoP structure on carbon nanotubes for flexible aqueous Zn batteries. The hierarchical microcrack structure improved electrolyte penetration and exposed sufficient active sites, resulting in a favorable capacity of 258.9 mA h g^{-1} at a current density of 2 A g^{-1}.[22] Zhao and co-workers developed an *in situ* interfacial modification strategy to create mesoporous NiCoP nanoarrays coated with ultrathin amorphous phosphate interfacial layers, achieving a high capacity of 358.3 mA h g^{-1} at 1 mA cm^{-2} in assembled alkaline Zn–metal batteries.[23] However, these fabricated devices often suffer from insufficient cycling stability. While considerable efforts have been devoted to developing electrolytes with intrinsic properties to enhance battery stability – such as facilitating the formation of a robust solid electrolyte interphase (SEI)[24] or exhibiting excellent chemical and thermal stability[25] – alkaline electrolytes still face challenges. These include issues with unstable cathode materials/structures and dendrite growth on Zn anodes.[26–28]

In this study, we employed an innovative photolithography technique combined with electro-deposition to introduce an ultrathin flexible 3D Ni micromesh (3D NM) as a current collector. This component, with its controllable and ordered lattices, provides a large specific surface area and a robust supporting framework for the subsequent uniform deposition of NiCoP, maximizing the exposure of electrochemically active materials to enhanced energy density. The as-designed material, characterized by high electrical conductivity and remarkable electrochemical activity, delivers a capacitance of 26.1 μA h cm^{-2} at a current density of 4 mA cm^{-2}. Additionally, atomic layer deposition (ALD) was applied to modify the surface of the Zn anode ($Zn@Al_2O_3@TiO_2$). The assembled flexible alkaline zinc batteries (3D NM@NiCoP// $Zn@Al_2O_3@TiO_2$) demonstrated excellent mechanical flexibility, with an areal capacity of 5.42 μA h cm^{-2} at a current density of 3 mA cm^{-2}. Notably, the device maintained 91% of its initial capacity over 11 000 charge–discharge cycles at 3 mA cm^{-2} in a 2 M KOH solution. This work provides a viable protocol for developing functional flexible electrodes on a large scale, paving the way for the practical application of the next generation of ultralight, ultrathin, and flexible wearable devices.

2 Results and discussion

2.1 Characterization of 3D NM@NiCoP and its electrochemical performance

The fabrication process for the flexible cathode, 3D NM@NiCoP, is illustrated in Fig. 1. It begins with spin-coating a photoresist layer onto a conductive ITO substrate (Fig. 1a). The coated layer is then exposed to UV light through a micromesh-patterned mask plate arranged in a honeycomb structure. This exposure induces a photochemical reaction in the illuminated areas, modifying their solubility compared to the unexposed regions. The unexposed regions are subsequently dissolved using a developer solution, accurately transferring the mask pattern onto the photoresist and forming a microgroove structure, as shown in Fig. 1b.

Next, nickel is electrodeposited into the microgrooves (Fig. 1c), producing a honeycomb-patterned Ni micromesh (NM) with a thickness of 7.5 μm and dimensions of 100 × 100 mm, which is peeled off from the residual photoresist (Fig. 1d). This Ni micromesh serves as the foundation for flexible electrodes, offering excellent optoelectronic properties and remarkable mechanical flexibility. To enhance conductivity and specific surface area, nanocone-shaped nickel structures are uniformly electrodeposited onto the Ni micromesh, resulting in a three-dimensional metallic nickel micromesh (3D NM) with a thickness of approximately 4 μm, as shown in Fig. 1e and Fig. S1a.†

In the final step, NiCoP is electrodeposited onto the 3D NM, forming the 3D NM@NiCoP structure and ensuring adequate exposure of electrochemically active NiCoP (Fig. 1f). The customizable nature of the micromesh allows for various configurations in terms of periodicity, line width, and pattern style, enabling precise control over optical transmission and electrical conductivity. Furthermore, the scalable electrodeposition technique supports the fabrication of large-area flexible electrodes, with the reusable electrodeposition solution significantly reducing cost and enhancing feasibility for broader applications.

Fig. 2 illustrates the morphology of the specimens at each fabrication step. Following the targeted deposition of Ni onto the indium tin oxide (ITO) substrate, the surface exhibits a sleek silver appearance, characterized by an evenly distributed array of honeycomb-shaped holes, as shown in Fig. 2a–c. A digital photograph of the self-supporting NM, with its transparent gray color, is provided in Fig. S2.† Afterwards, the honeycomb holes in the NM become smaller while maintaining the overall array structure. The initially smooth surface is uniformly covered with nickel nanocones, as evidenced in Fig. 2d–f, confirming the successful electrodeposition of nickel nanocone arrays onto the NM. The process forms a 3D interconnected conductive network (3D NM), which enhances the electrode's capacity due to a high mass of active materials. Further electrodeposition leads to the formation of 3D NM@NiCoP, characterized by its dark gray hue, as depicted in Fig. 2g–i. Additionally, Energy Dispersive X-ray (EDX) spectroscopy mapping in Fig. S3† demonstrates the uniform distribution of Ni, Co, and P elements throughout the micromesh structure, confirming the even deposition of NiCoP onto the 3D NM. The well-defined architecture of 3D NM@NiCoP enhances the exposure of electrochemically active sites and promotes efficient contact between the active materials and electrolyte, contributing significantly to improved electrochemical performance.

To investigate the effect of the 3D structure, an *I–V* method was employed to compare the electrical conductivity of Ni micromesh, 3D NM and 3D NM@NiCoP. As shown in Fig. 3a, the *I–V* curves for 3D NM and 3D NM@NiCoP exhibit steeper slopes compared to that of the nickel micromesh, indicating superior conductivity. This finding is further supported by the

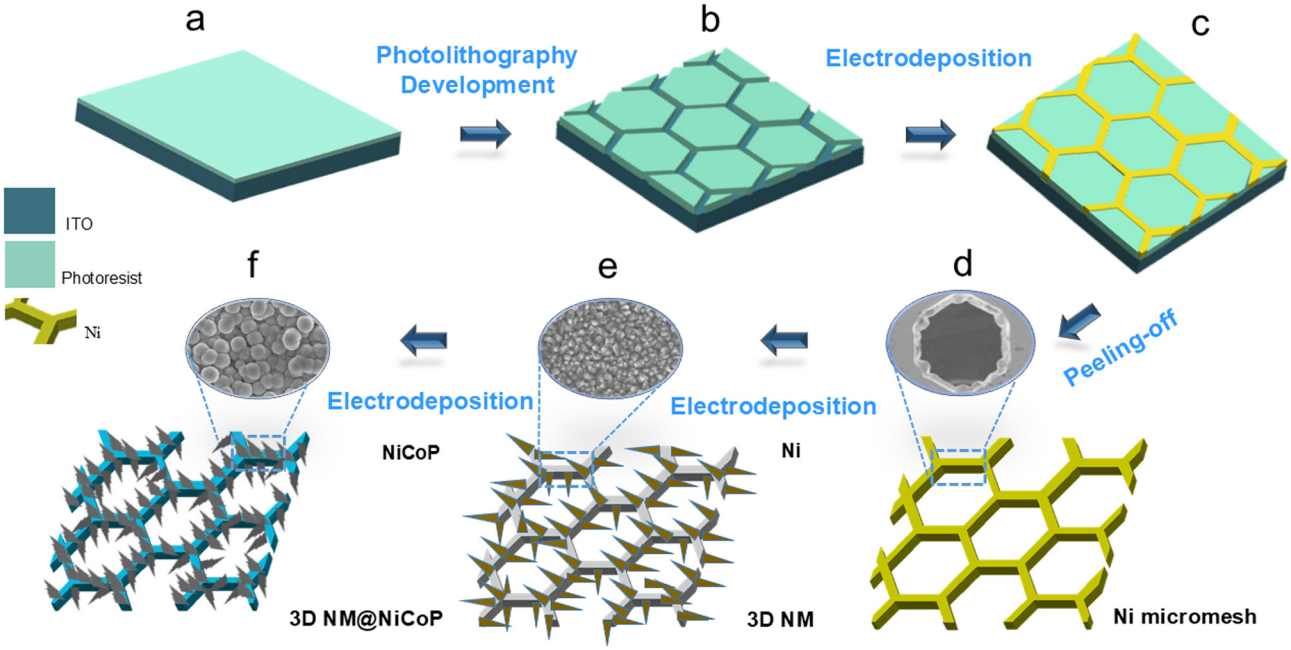

Fig. 1 Schematic illustration of the cathode fabrication process: (a) a photoresist layer coated on the ITO substrate, (b) a patterned photoresist developed onto the ITO substrate *via* photolithography, (c) Ni selectively electrodeposited onto the patterned ITO substrate, (d) a Ni micromesh obtained by peeling off the residual photoresist, (e) a 3D nickel micromesh (3D NM) obtained by electrodepositing Ni nanocones onto the nickel micromesh, and (f) NiCoP electrodeposited onto the 3D NM structure.

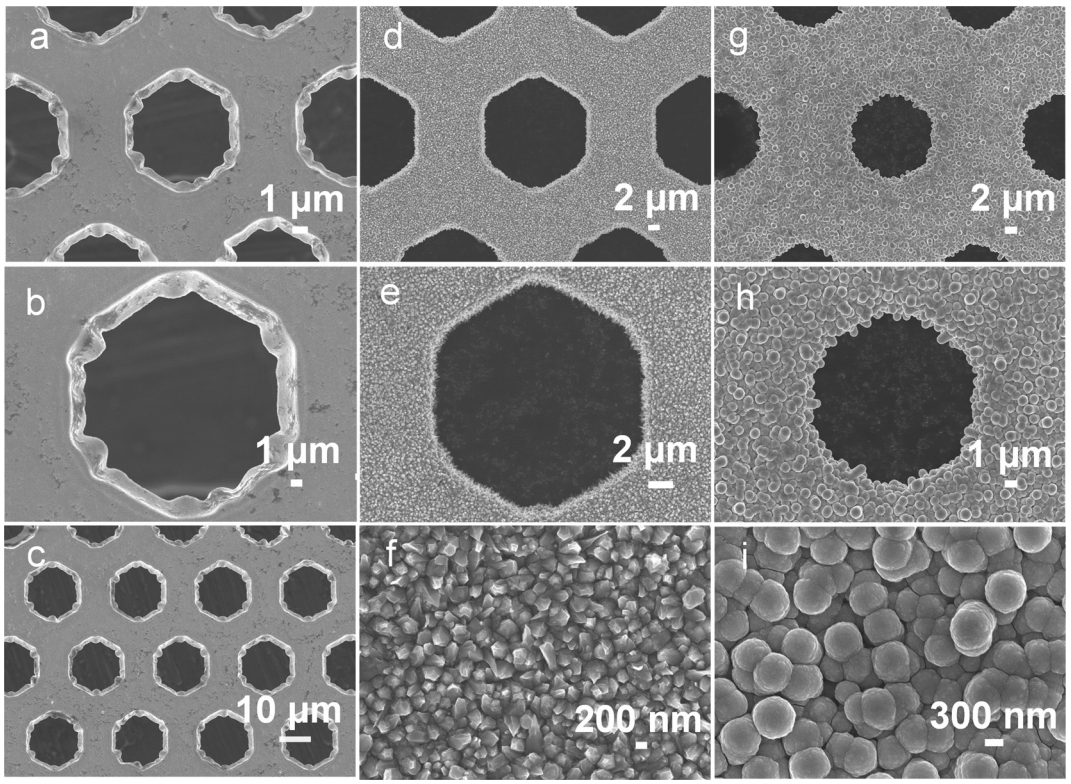

Fig. 2 SEM images illustrating the morphologies of the as-prepared samples at different stages: (a–c) Ni micromesh. (d–f) 3D Ni micromesh. (g–i) 3D NM@NiCoP at various magnifications.

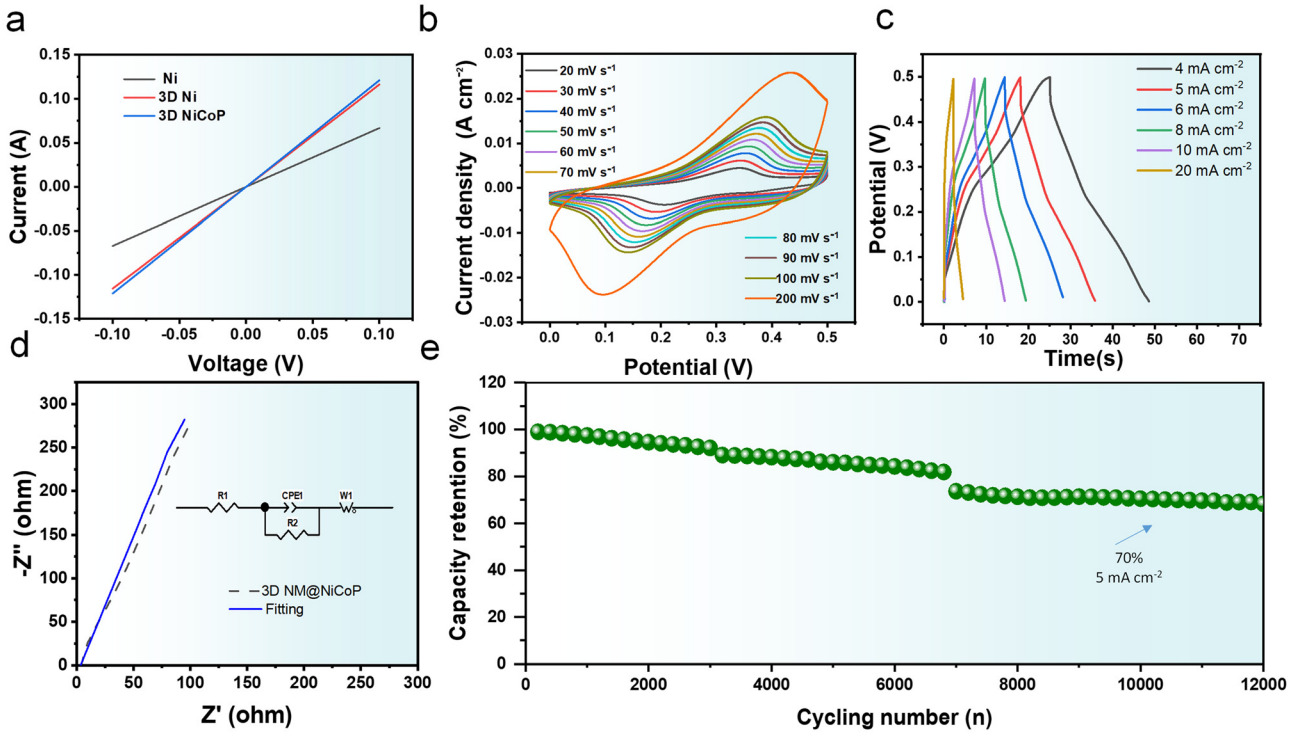

Fig. 3 Electrochemical performance of the 3D NM@NiCoP: (a) *I–V* curves for Ni, 3D NM and 3D NM@NiCoP with the same area (1 × 1 cm^{-2}), (b) cyclic voltammetry (CV) curves of 3D NM@NiCoP at scan rates ranging from 20 to 200 mV s^{-1}, (c) galvanostatic charge–discharge (GCD) curves of 3D NM@NiCoP at current densities between 4 and 20 mA cm^{-2}, (d) Nyquist impedance spectrum of 3D NM@NiCoP, and (e) long-term cycling performance of 3D NM@NiCoP at 5 mA cm^{-2}.

data presented in Fig. S4,† which reveal sheet resistance values of 0.13 Ω sq^{-1} for the NM electrode and 0.044 Ω sq^{-1} for the 3D NM electrode. To analyze the crystalline structure of Ni, 3D NM and 3D NiCoP, XRD analysis was performed and the results are presented in Fig. S5a.† All three patterns display distinct diffraction peaks at 44.9°, 51.2° and 76.5°, corresponding well to Ni (JCDPS no. 04-0850), confirming the successful deposition of metallic Ni. However, no peaks corresponding to NiCoP are observed, suggesting that the synthesized active material has an amorphous structure. Alternatively, the Raman spectrum of 3D NM@NiCoP, as shown in Fig. S5b,† displays distinct peaks at 480, 520, and 685 cm^{-1}. These peaks, combined with the EDX mapping results in Fig. S3,† further validate the successful deposition of NiCoP on the surface of the 3D NM.[29]

To evaluate the electrochemical properties of 3D NM@NiCoP, cyclic voltammetry (CV), galvanostatic charge/discharge (GCD) and electrochemical impedance spectroscopy (EIS) were conducted using a three-electrode system in 2 M KOH. A platinum plate served as the counter electrode, Ag/AgCl as the reference electrode, and 3D NM@NiCoP as the working electrode. Fig. 3b shows the CV curves of 3D NM@NiCoP at scan rates ranging from 20 to 200 mV s^{-1} within a voltage window of 0 to 0.5 V. Symmetric redox peaks are observed as the scan rate increases, with no significant deformation, indicating the pseudocapacitive behavior of the NiCoP electrode. The redox reaction of the NiCoP electrode can be summarized as follows:[30]

$$NiCoP + OH^- \leftrightarrow NiCoPOH + e^- \quad (1)$$

$$NiCoPOH + OH^- \leftrightarrow NiCoPO + H_2O + e^- \quad (2)$$

The 3D NM@ NiCoP electrode displays distinct redox peaks that remain well-defined even at a scan rate of 200 mV s^{-1}, suggesting swift electron and ion transport as well as high reversibility of redox reactions within the electrode. The GCD curves of the 3D NM@NiCoP electrode were measured at various current densities (4, 5, 6, 8, 10 and 20 mA cm^{-2}) (Fig. 3c), and the corresponding areal capacities were calculated from the GCD curves (Fig. S6a†). At a current density of 4 mA cm^{-2}, 3D NM@NiCoP delivers an areal capacitance of 26.1 μA h cm^{-2}. All GCD curves demonstrate high symmetry, indicating excellent coulombic efficiency during charge/discharge processes. Notably, the areal capacitance surpasses those of numerous previous studies on transition metal-based electrodes, as shown in Fig. S6b and Table S1.†

To further investigate the ion diffusion kinetics of the 3D NM@NiCoP electrodes, EIS measurements were conducted over a frequency range of 100 kHz–0.01 Hz, as depicted in Fig. 3d. Fitting the EIS data to the equivalent circuit model

yielded an internal resistance (R_s) of 3.08 Ω and a charge transfer resistance (R_{ct}) of 0.31 Ω. This low impedance of the electrode material confirmed the electrode's fast electron transfer during charge–discharge processes. Additionally, the cycling stability of the 3D NM@NiCoP electrode was evaluated at a current density of 5 mA cm^{-2}, revealing good durability with a capacity retention of 84% after 6000 cycles and 70% after 10 000 cycles of charge–discharge processes (Fig. 3e). The stability surpasses that of other comparable electrodes such as NiCoP/NF[31] NiCoP/$NiCO_2S_4$[19] and 3D NM@NiCo BH.[32] The desirable electrochemical performance and long cycle life of 3D NM@NiCoP can be attributed to the mechanical stability and excellent electrical conductivity of the 3D NM framework. The heterogeneous structure provides a large effective surface area to support high NiCoP loading, thereby facilitating rapid and ample redox reactions.

2.2 Assembled Zn@Al_2O_3@TiO_2//3D NM@NiCoP devices and their electrochemical properties

To explore the practical application of 3D NM@NiCoP, a zinc-ion battery full cell was assembled using 3D NM@NiCoP as the cathode and ALD-coated Zn as the anode. The structure and properties of the modified anodes were thoroughly analyzed. Initially, zinc foil was coated with a 20 nm layer of TiO_2 *via* ALD to reduce corrosion and mitigate side reactions at the Zn anode. The amorphous TiO_2 layer was chosen for its electrochemical and chemical stability as a protective coating for the anode.[33,34] The fabrication process of the anode is illustrated in Fig. S7.† Cleaned Zn samples were placed in a preheated ALD chamber, where a vacuum pump established the required conditions within the reaction chamber. Subsequently, thin films of titanium dioxide (TiO_2) were deposited onto the zinc substrates, creating Zn@TiO_2. The digital photograph in Fig. S8† shows the color changes of the Zn foil before and after ALD. SEM images clearly depict the morphology and cross-sectional views, revealing the presence of a TiO_2 thin film on the treated Zn foil, distinguishing it from the untreated counterpart (Fig. 4a–d). Cleaning the Zn foil before coating is proved essential for maintaining the integrity of the TiO_2 layer on the Zn surface in KOH solution, as evidenced by the digital photograph in Fig. S9.†

Based on the Zn@TiO_2 anode, the electrochemical performance of its assembled full cell with the synthesized 3D NM@NiCoP cathode (Zn@TiO_2//3D NM@NiCoP) was preliminarily tested in 2 M KOH. Fig. S10a† displays the CV curves at scan rates ranging from 3 to 50 mV s^{-1} within a voltage window of 1.55–1.95 V. Quasi-symmetric redox peaks, with increasing scan rate, are observed, indicating the pseudocapacitive behavior of the Zn@TiO_2//3D NM@NiCoP device. The well-maintained curve shapes, even at the highest scan rate of 50 mV s^{-1}, suggest excellent reversibility and good rate performance of the redox reactions. The gradually separated anodic and cathodic peaks further demonstrate polarization. Besides, the supercapacitive behavior of the device is sup-

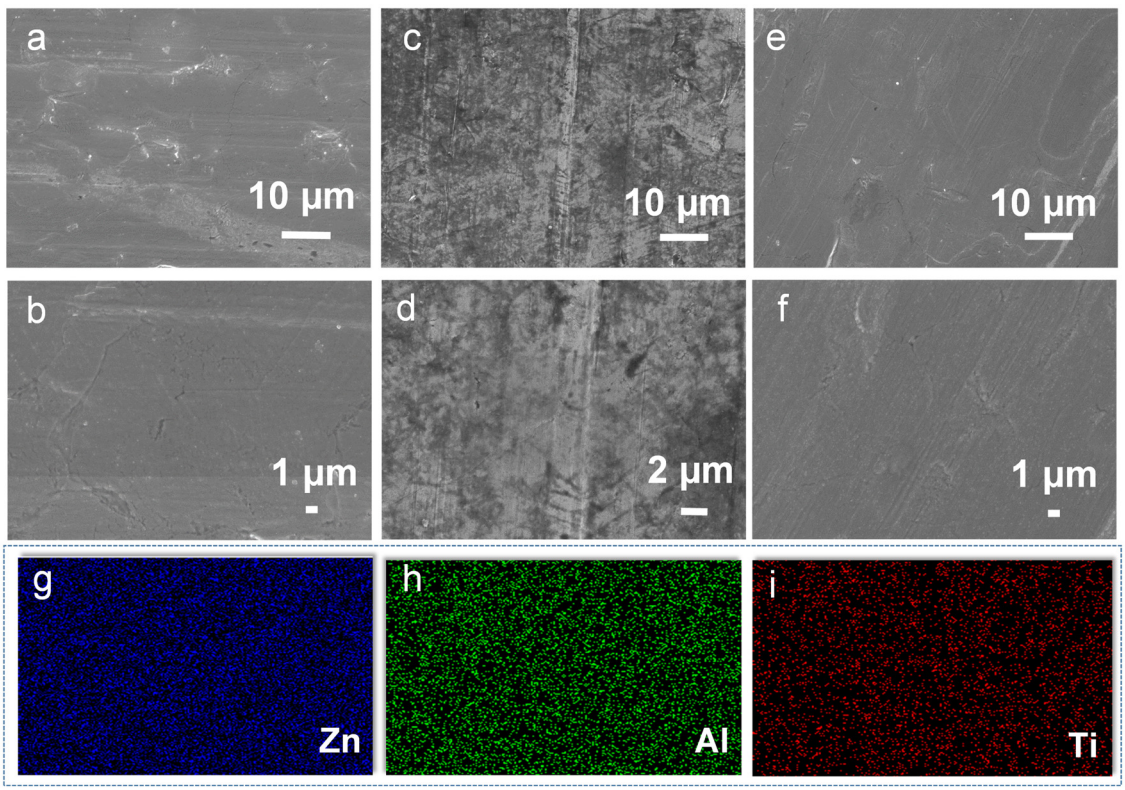

Fig. 4 SEM images at different magnifications: (a and b) cleaned Zn foil, (c and d) TiO_2 coating, (e and f) Al_2O_3 coating, and (g–i) elemental mapping of Zn@Al_2O_3@TiO_2.

ported by the GCD curves, shown in Fig. S10b,† which exhibit quasi-triangle-like shapes without distinct voltage platforms. Electrochemical impedance spectroscopy (EIS) measurements over a frequency range of 100 kHz to 0.01 Hz (Fig. S10c†) reveal relatively low impedance for the Zn@TiO_2//3D NM@NiCoP cell. However, long-term cycling stability, assessed by GCD at a current density of 3 mA cm^{-2} (Fig. S10d†), shows an average capacity of 3.5 μA h cm^{-2} with 93% capacity retention after 4000 cycles. Further investigation revealed that the Zn@TiO_2 anode displayed low resistance to corrosion and had a limited lifespan in the KOH solution, with pronounced hydrogen evolution as evidenced in Fig. S11.†

To further improve the electrochemical performance of the device, a modified anode, Zn@Al_2O_3@TiO_2, was developed with an Al_2O_3 layer positioned between the Zn and TiO_2 coatings (Fig. S12†). This dense Al_2O_3 layer is designed to prevent side reactions between the electrolyte and Zn during charge/discharge cycles, effectively suppressing the formation of passivation layers on the Zn anode surface. It is also well known that the Al_2O_3 layer facilitates an activation mechanism for the Zn anode during initial cycles.[33–35] Additionally, electronic conductivity measurement using the *I–V* method (Fig. S13†) indicates improved conductivity for the Zn@Al_2O_3@TiO_2 electrodes, benefitting from the 3D structure of conductive interconnects.

SEM images also display the surface morphology of the anode after coating with Al_2O_3 (Fig. 4e and f). The ALD-applied layer effectively smoothed the surface and completely covered the pores and exposed areas, with no visible pinholes. The 10 nm Al_2O_3 layer successfully seals defects, enhancing the anode's stability. To investigate the wettability of various electrodes, contact angle measurements were conducted by dropping water droplets onto the electrode surfaces. Notably, the Zn@Al_2O_3@TiO_2 electrode exhibited significantly enhanced wettability, with an initial contact angle of 39.15°, much lower than those of Zn@TiO_2 (48.8°) and bare zinc (88.5°), as shown in Fig. S14.†

Energy dispersive X-ray spectroscopy (EDX) analysis and corresponding elemental mappings confirm the presence of Zn, Al and Ti on the modified Zn anode surface (Fig. 4g–i). In Fig. S15,† the diffraction patterns correspond well to the characteristic peaks of Zn (JCDPS no. 87-0713) at 2θ = 35.6°, 38.3°, 42.8°, 53.8° and 69.3°. The absence of peaks for Al_2O_3 and TiO_2 may be attributed to their minimal quantities or the fact that the low-temperature ALD coating layer exists in an amorphous form, consistent with our previous study.[36]

Afterwards, an alkaline Zn ion battery was constructed using the improved Zn@Al_2O_3@TiO_2 anode and the 3D NM@NiCoP cathode (Fig. 5a). The electrochemical performance of this assembled device was evaluated in a 2 M KOH. First, CV was performed over a voltage window of 1.4 to 1.95 V, with scan rates increasing from 1 to 80 mV s^{-1} (Fig. 5b). The CV curves exhibited characteristic rectangular shapes and well-defined faradaic redox peaks without significant distortion,

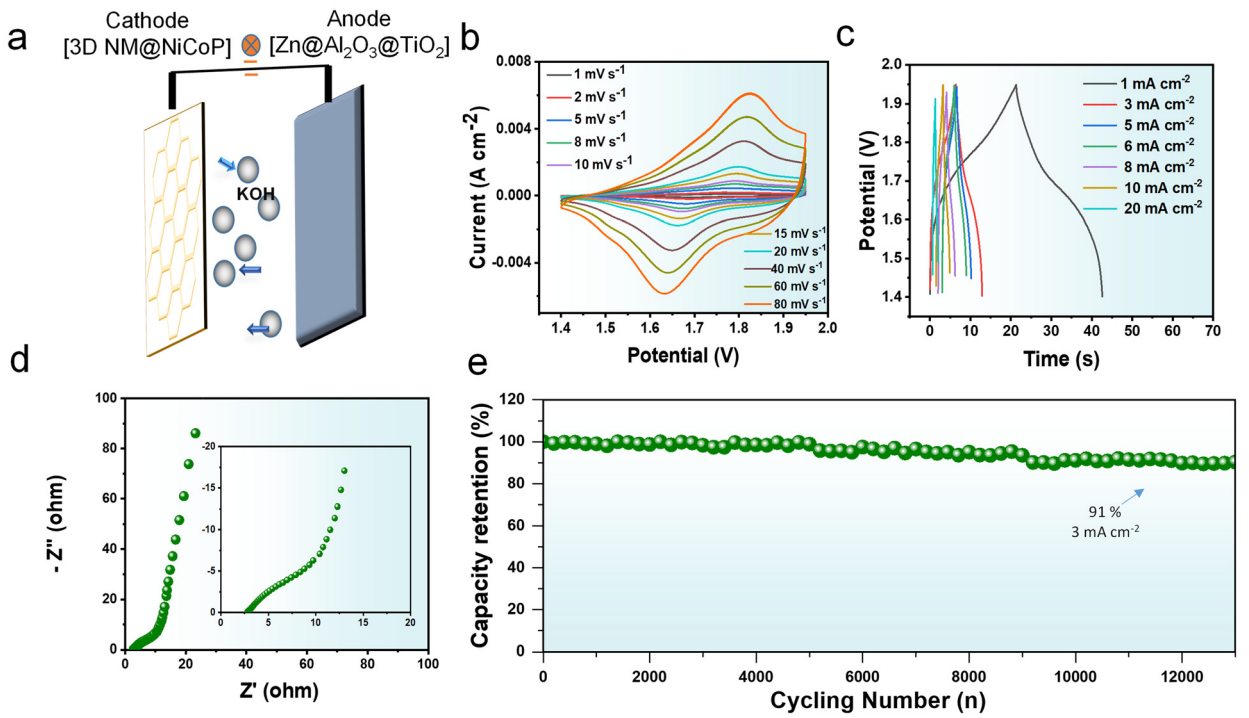

Fig. 5 Electrochemical performance of Zn@Al_2O_3@TiO_2//3D NM@NiCoP in 2 M KOH: (a) the assembled anode and cathode in a two-electrode setup in 2 M KOH. (b) Cyclic voltammetry (CV) curves at various scan rates. (c) Galvanostatic charge–discharge (GCD) curves at different current densities. (d) EIS measured over a frequency range of 0.01 Hz–100 kHz. (e) Cycling stability of Zn@Al_2O_3@TiO_2//3D NM@NiCoP at a current density of 3 mA cm^{-2}.

even at a high scan rate of 80 mV s^{-1}. GCD curves were recorded at current densities from 1 to 20 mA cm^{-2} within the same voltage window (Fig. 5c). The nearly symmetric shapes indicate rapid and reversible electrochemical reactions, with extended discharge times suggesting improved energy storage capacity. Consequently, the device achieved an areal capacity of 5.42 μA h cm^{-2} at a current density of 3 mA cm^{-2}, surpassing several recently published flexible devices such as AgNW@NiCo/$NiCo(OH)_2$//Ag NW/graphene,[37] MnO-NP/ITO-NP//MnO-NP/ITO-NP,[38] Ni–Co–N/GP//GOP,[39] and Cu@Ni@NiCoS//NFs[40] (see Fig. S16a and Table S2†). Furthermore, EIS of the Zn@Al_2O_3@TiO_2//3D NM@NiCoP device was conducted across a frequency range of 0.01 Hz to 100 kHz. The Nyquist plot (Fig. 5d) shows a short high-frequency arc and a steep slope in the low frequency, indicating rapid electrochemical kinetics and efficient ion transport. Additionally, long-term cycling stability was evaluated by subjecting the device to continuous charging and discharging cycles at a high current density of 3 mA cm^{-2} (Fig. 5e). Remarkably, the device retained 91% of its initial capacity after 11 000 cycles, outperforming the stability of the Zn@TiO_2 anode device under identical conditions (Fig. S16b†). This stability exceeds those of other devices in recently published relevant work (see Table S3†). In addition, a flexible zinc ion battery with multifunctional integration can be realized by designing embedded stretchable electrodes.[40]

3 Conclusion

In conclusion, an ultrathin, ultralight and flexible 3D NM@NiCoP was successfully fabricated through a combination of photolithography and electro-deposition techniques. This self-standing electrode achieved a remarkable areal capacity of 26.1 μA h cm^{-2} at a current density of 4 mA cm^{-2}, driven by the rapid electron and ion transportation enabled by the highly conductive 3D NM current collector and the extensive exposure of the active NiCoP material, facilitating efficient redox reactions. Paired with a surface-modified hydrophilic Zn@Al_2O_3@TiO_2 anode, the resulting Zn-ion battery (Zn@Al_2O_3@TiO_2//3D NM@NiCoP) demonstrated outstanding cycling stability, retaining 91% of its initial capacity after 11 000 cycles. This device offers significant potential for a broad range of energy storage applications, combining low cost and scalable production with particular suitability for wearable technologies.

Data availability

The data supporting this article have been included as part of the ESI.†

Conflicts of interest

There are no conflicts of interest to declare.

Acknowledgements

The authors are grateful for the financial support from the National Natural Science Foundation of China (Grant No. U22A20193 and 52175534), the National Key Research and Development Program of China (Grant No. 2023YFB4606100), the Natural Science Foundation of Hunan Province, China (Grant No. 2024JJ2018), and the Science and Technology Innovation Program of Hunan Province (Grant No. 2021RC3052).

References

1 C. Yang, J. Chen, X. Ji, T. P. Pollard, X. Lü, C.-J. Sun, S. Hou, Q. Liu, C. Liu, T. Qing, Y. Wang, O. Borodin, Y. Ren, K. Xu and C. Wang, *Nature*, 2019, **569**, 245–250.
2 J. Zhang, W. Li, J. Wang, X. Pu, G. Zhang, S. Wang, N. Wang and X. Li, *Angew. Chem., Int. Ed.*, 2023, **62**, e202215654.
3 Y. Xu, G. Zhang, J. Liu, J. Zhang, X. Wang, X. Pu, J. Wang, C. Yan, Y. Cao, H. Yang, W. Li and X. Li, *Energy Environ. Mater.*, 2023, **6**, e12575.
4 X. Chen, W. Li, D. Reed, X. Li and X. Liu, *Electrochem. Energy Rev.*, 2023, **6**, 33.
5 T. Bashir, S. Zhou, S. Yang, S. A. Ismail, T. Ali, H. Wang, J. Zhao and L. Gao, *Electrochem. Energy Rev.*, 2023, **6**, 5.
6 T. H. Wu, Y. Zhang, Z. D. Althouse and N. Liu, *Mater. Today Nano*, 2019, **6**, 100032.
7 X. Guo and G. He, *J. Mater. Chem. A*, 2023, **11**, 11987–12001.
8 H. Dong, J. Li, J. Guo, F. Lai, F. Zhao, Y. Jiao, D. J. L. Brett, T. Liu, G. He and I. P. Parkin, *Adv. Mater.*, 2021, **33**, 2007548.
9 J. Liu, C. Guan, C. Zhou, Z. Fan, Q. Ke, G. Zhang, C. Liu and J. Wang, *Adv. Mater.*, 2016, **28**, 8732–8739.
10 Y. Zhang, P. Wang, X. Dong, H. Jiang, M. Cui and C. Meng, *Fundam. Res.*, 2023, **3**, 288–297.
11 Y. Zeng, Y. Meng, Z. Lai, X. Zhang, M. Yu, P. Fang, M. Wu, Y. Tong and X. Lu, *Adv. Mater.*, 2017, **29**, 1702698.
12 H. Chen, Z. Shen, Z. Pan, Z. Kou, X. Liu, H. Zhang, Q. Gu, C. Guan and J. Wang, *Adv. Sci.*, 2019, **6**, 1802002.
13 G. Zhang, H. Yang, H. Zhou, T. Huang, Y. Yang, G. Zhu, Y. Zhang and H. Pang, *Angew. Chem., Int. Ed.*, 2024, **63**, e202401903.
14 Y. Xie, B. Fei, D. Cai, Q. Chen, Z. Cui, Q. Wang and H. Zhan, *Energy Storage Mater.*, 2020, **31**, 27–35.
15 K. Zhou, S. Wang, G. Zhong, J. Chen, Y. Bao and L. Niu, *Small*, 2022, **18**, 2202799.
16 S. Zhao, G. Qu, C. Wang, Y. Zhang, C. Li, X. Li, J. Sun, J. Leng and X. Xu, *Nanoscale*, 2021, **13**, 18586–18595.
17 W. Liu, Y. Chen, Y. Wang, Q. Zhao, L. Chen, W. Wei and J. Ma, *Energy Storage Mater.*, 2021, **37**, 336–344.
18 L. Feng and H. Xue, *ChemElectroChem*, 2017, **4**, 20–34.
19 F. Yang, Y. Shen, Z. Cen, J. Wan, S. Li, G. He, J. Hu and K. Xu, *Sci. China Mater.*, 2022, **65**, 356–363.

20 Z. Nie, W. Yan, H. Yu, Y. Zhang, M. Tian, X. Zhang, Y. Xiong, P. Cao and G. Zhang, *Composites Part B: Engineering*, 2025, **289**, 111934.
21 M. Li, M. Zhao, S. Mourdikoudis, Q. Zheng, L. Jiao, Z. Su, M. Shi, Q. Wang, Y. Wu and S. Yang, *J. Power Sources*, 2023, **580**, 233333.
22 H. Wang, Y. Lu, Z. Nie, H. Liu, B. Dai, X. Shi, B. Yan, T. Zhao, Z. Zhang, J. Zhu and Y. Zhao, *Small*, 2023, **19**, 2206338.
23 S. Zhao, G. Qu, C. Wang, X. Zhang, X. Wang, P. Hou, G. Zhao, J. Leng, X. Xu and T. Zhai, *Chem. Eng. J.*, 2023, **461**, 141790.
24 D. Zhang, H. Fu, X. Ma, X. Yu, F. Li, J. Zhou and B. Lu, *Angew. Chem., Int. Ed.*, 2024, **63**, e202405153.
25 X. Yi, H. Fu, A. M. Rao, Y. Zhang, J. Zhou, C. Wang and B. Lu, *Nat. Sustain.*, 2024, **7**, 326–337.
26 X. Li, Z. Chen, P. Ruan, X. Hu, B. Lu, X. Yuan, S. Tian and J. Zhou, *Nanoscale*, 2024, **16**, 2923–2930.
27 C. Li, S. Zhao, X. Zhang, G. Qu, X. Li, N. Li, T. Wang, J. Leng, C. Wang and X. Xu, *Chem. Eng. J.*, 2022, **450**, 137998.
28 S. Yang, C. Li, Y. Wang, S. Chen, M. Cui, X. Bai, C. Zhi and H. Li, *Energy Storage Mater.*, 2020, **33**, 230–238.
29 J. Qian, L. Sun, X. Shi, L. Wu, S. Su, K. Wang and Y. Zhang, *Chem. Eng. J.*, 2022, **429**, 132482.
30 W. Song, J. Wu, G. Wang, S. Tang, G. Chen, M. Cui and X. Meng, *Adv. Funct. Mater.*, 2018, **28**, 1804620.
31 M. Kong, Z. Wang, W. Wang, M. Ma, D. Liu, S. Hao, R. Kong, G. Du, A. M. Asiri, Y. Yao and X. Sun, *Chem. – Eur. J.*, 2017, **23**, 4435–4441.
32 G. Zhang, J. Hu, Y. Nie, Y. Zhao, L. Wang, Y. Li, H. Liu, L. Tang, X. Zhang, D. Li, L. Sun and H. Duan, *Adv. Funct. Mater.*, 2021, **31**, 2100290.
33 H. Sopha, G. D. Salian, R. Zazpe, J. Prikryl, L. Hromadko, T. Djenizian and J. M. Macak, *ACS Omega*, 2017, **2**, 2749–2756.
34 K. Zhao, C. Wang, Y. Yu, M. Yan, Q. Wei, P. He, Y. Dong, Z. Zhang, X. Wang and L. Mai, *Adv. Mater. Interfaces*, 2018, **5**, 1800848.
35 H. He, H. Tong, X. Song, X. Song and J. Liu, *J. Mater. Chem. A*, 2020, **8**, 7836–7846.
36 D. Wei, Y. Wu, Y. Nie, J. Duan, C. Cao, J. Wu, L. Li, Z. Chen, G. Zhang and H. Duan, *Appl. Surf. Sci.*, 2020, **529**, 147114.
37 J. Liu, G. Shen, S. Zhao, X. He, C. Zhang, T. Jiang, J. Jiang and B. Chen, *J. Mater. Chem. A*, 2019, **7**, 8184–8193.
38 J. Choi, D. Nam, D. Shin, Y. Song, C. H. Kwon, I. Cho, S. W. Lee and J. Cho, *ACS Nano*, 2019, **13**, 12719–12731.
39 F. Liu, L. Zeng, Y. Chen, R. Zhang, R. Yang, J. Pang, L. Ding, H. Liu and W. Zhou, *Nano Energy*, 2019, **61**, 18–26.
40 B. S. Soram, I. S. Thangjam, J. Y. Dai, T. Kshetri, N. H. Kim and J. H. Lee, *Chem. Eng. J.*, 2020, **395**, 125019.